

Supporting information

Electrical molecular switch addressed by chemical stimuli

*H. Audi,¹ Y. Viero,² N. Alwhaibi,³ Z. Chen,¹ M. Iazykov,¹ A. Heynderickx,¹ F. Xiao,¹
D. Guérin,² C Krzeminski,² I.M. Grace,³ C.J. Lambert,^{3,*} O. Siri,^{1,*} D.Vuillaume^{2,*},
S Lenfant^{2,*}, H. Klein^{1,*}*

1) Centre Interdisciplinaire de Nanoscience de Marseille (CINaM), CNRS, Aix
Marseille Université, Marseille, France.

2) Institut d'Electronique, Microélectronique et Nanotechnologie (IEMN), CNRS,
Université de Lille, Avenue Poincaré, Villeneuve d'Ascq, France.

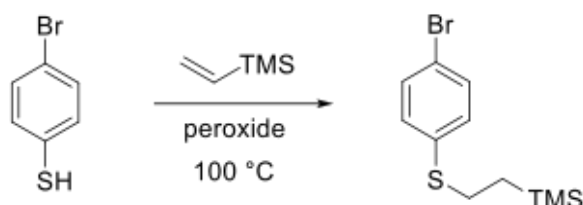
3) Physics Department, Lancaster University, Lancaster, LA1 4YB (UK).

I	Synthesis.....	S2
II	Mechanically Controlled Break Junction (MCBJ).....	S6
III	XPS measurements.....	S10
IV	Measurements on ^{Au} TS/SAM/C-AFM tip junctions.....	S13
V	C-AFM on NMJs.....	S17
VI	MCBJ measurements.....	S18
VII	Modeling molecule gas phase.....	S22
VIII	Modeling electron transport in metal/molecule/metal junction.....	S28
IX	References.....	S32

I. Synthesis.

- *Synthesis of 4.*

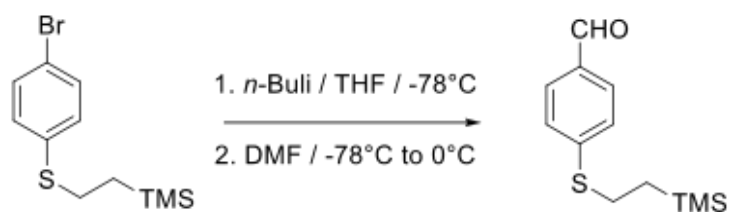
Step 1:



The target compound was prepared as reported¹⁻² using a modified procedure. To a Schlenk tube was added 6.9 g (36.49 mmol) of 4-bromothiophenol, 6.6 ml (42.82 mmol) of vinyltrimethylsilane, and 0.95 ml (5.05 mmol) tert-butyl peroxide under argon. The reaction mixture was stirred at 100°C for 10 h. The reaction mixture was diluted by adding 200 ml of hexane, and the obtained solution was washed once with a 10% sodium hydroxide aqueous solution. The organic layer was separated, dried (MgSO₄), and then concentrated under reduced pressure. The crude product was purified by column chromatography over silica gel (eluent: cyclohexane) to afford the target protected thiol as a yellow oil (m = 8.6 g, 83% yield).

¹H NMR (400 MHz, CDCl₃): δ(ppm) 7.38 (d, J = 8.6 Hz, 2H), 7.15 (d, J = 8.5 Hz, 2H), 2.96 – 2.88 (m, 2H), 0.93 – 0.87 (m, 2H), 0.03 (s, 9H).

Step 2 :



A solution of 2-(trimethylsilyl)ethyl-4-bromophenyl sulfide ($m = 1,0$ g, 3.46 mmol) in 30 ml of dry THF was treated with n-BuLi ($v = 1.7$ ml of a 2.5M solution in hexane, 4.25 mmol) dropwise under argon at -78 °C. After stirring for 1h, the reaction mixture was quenched with anhydrous dimethylformamide ($v = 0.33$ ml, 4.15 mmol) at -78 °C. The mixture was then further stirred for an hour at low temperature, an additional hour at room temperature, and poured into aqueous NH_4Cl . The mixture was extracted with CH_2Cl_2 (2×30 ml). The combined organic layers were washed with water, dried (MgSO_4) and filtered. The solvent was evaporated under reduced pressure, and the crude product was purified by column chromatography over silica gel (eluent: CH_2Cl_2 : PE=3:1) to afford **4** ($m = 0.60$ g, 73% yield) as a colorless oil.

^1H NMR (400 MHz, CDCl_3): δ (ppm) 9.90 (s, 1H), 7.74 (d, $J = 8.3$ Hz, 2H), 7.31 (d, $J = 8.3$ Hz, 2H), 3.12 – 2.93 (m, 2H), 1.04 – 0.87 (m, 2H), 0.06 (s, 9H). ^{13}C NMR (CDCl_3): δ (ppm) 191.46, 147.62, 133.22, 130.20, 126.45, 77.55, 77.23, 76.91, 28.00, 16.43, -1.56.

- *Synthesis of 5.*

To a solution of **4** ($m = 113$ mg, 0.47 mmol) in 3ml of ethanol was added the Bandrowski base **2** ($m = 70$ mg, 0.22 mmol) and two drops of piperidine. The mixture was refluxed for 24h. The resulting precipitate was filtered, washed with ethanol and dried to give the desired product **5** as beige solid ($m = 65$ mg, 43% yield).

^1H NMR (250 MHz, DMSO-d_6): δ (ppm) 0.04 (s, 18H); 0.83-0.90 (m, 4H); 2.98-3.05 (m, 4H); 5.50 (s, 4H); 6.71-6.75 (4H, d, $J = 8.5$ Hz); 7.05-7.09 (2H, d, $J = 8.5$ Hz); 7.23-7.26 (m, 6H); 7.52-7.56 (4H, d, $J = 8.25$ Hz). ESI-HRMS:

Calculated for $\text{C}_{42}\text{H}_{48}\text{N}_6\text{S}_2\text{Si}_2$, 756.2920 ; Found 757.2989 $[\text{M}+\text{H}]^+$.

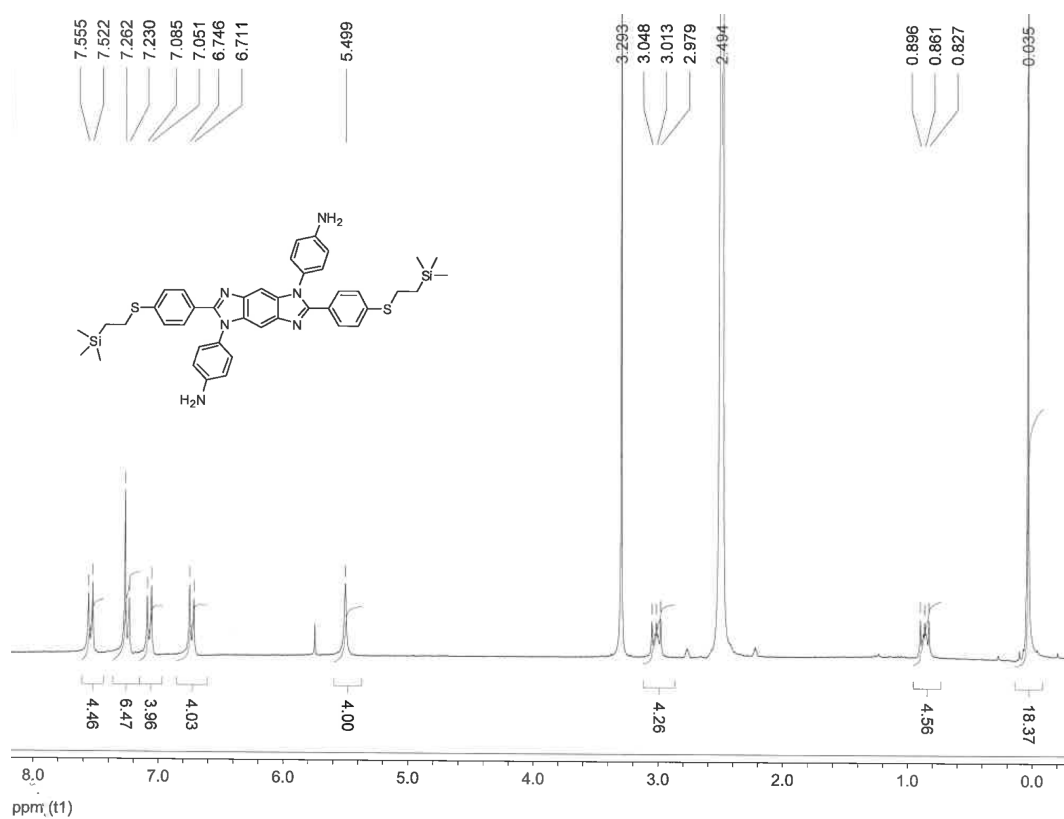


Figure S1-a. ^1H NMR spectrum of **5** in DMSO.

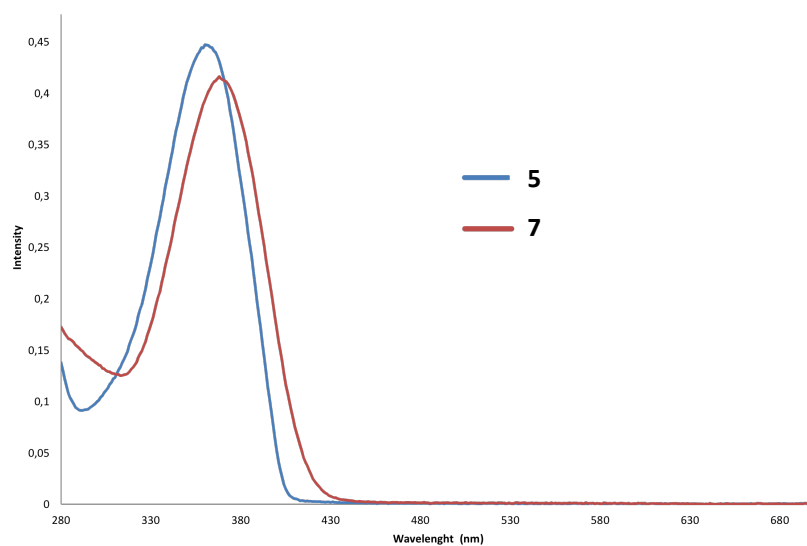


Figure S1-b. UV-vis absorption of **5** ($C = (1.88 \times 10^{-5} \text{M})$, $\lambda_{\text{max}} = 360 \text{ nm}$) and its protonated form **7** ($\lambda_{\text{max}} = 368 \text{ nm}$) in THF.

- *Synthesis of 6.*

To a solution of **4** (m = 100 mg, 0.73 mmol) in 3ml of ethanol was added reagent **3** (m = 87.6 mg, 0.37 mmol) and three drops of piperidine. The mixture was refluxed for 24h. The resulting precipitate was filtered, washed with ethanol and dried to afford **6** as beige solid (m = 105 mg; 49%).

¹H NMR (400 MHz, DMSO-d₆): δ(ppm) 12.59 (d, J = 17.7 Hz, 2H), 8.04 (d, J = 12.9 Hz, 4H), 7.76 (s, 1H), 7.59 (s, 1H), 7.37 (d, J = 13.6 Hz, 4H), 3.08 – 2.97 (m, 4H), 0.92 – 0.78 (m, 4H), 0.00 (s, 18H). ESI-HRMS: Calculated for C₃₀H₃₈N₄S₂Si₂, 574.2076 ; Found 575.2147 [M+H]⁺.

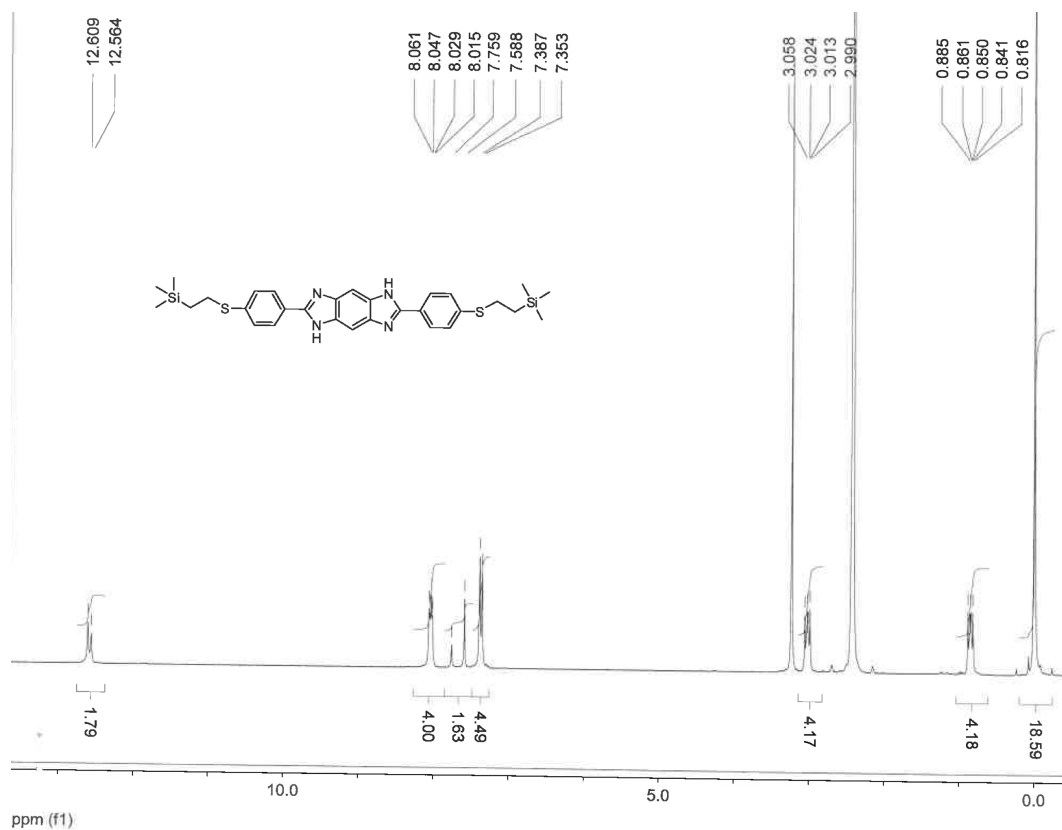


Figure S1-c. ¹H-NMR spectrum of **6** in DMSO.

II. Mechanically Controlled Break Junction (MCBJ).

MCBJ set-up.

The MCBJ, as introduced by Muller et al.³ consists in stretching a metallic wire by bending an elastic substrate supporting the wire with a mechanical actuator until the junction breaks, giving two separate electrodes. The electrode separation can then be adjusted by a feedback loop using the current flowing through the junction. MCBJ exhibits excellent mechanical stability, which results from the reduction of the mechanical loop connecting one electrode to the other. For this study, our MCBJ is operated at room temperature in organic solutions.

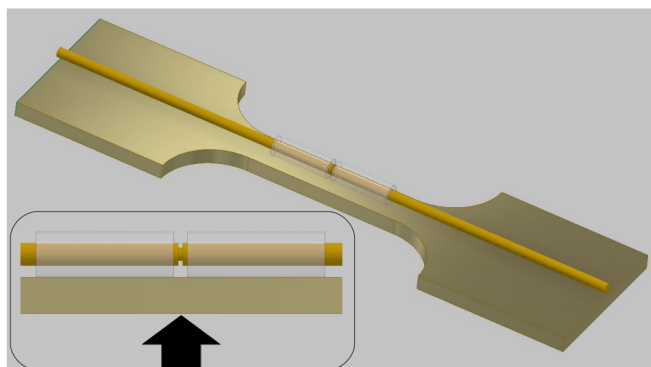


Figure S2 : *Schematic of the sample used for our MCBJ. The samples are made from Au wire glued into two quartz capillaries which are then glued onto a phosphorous bronze bending beam. As seen in the inset, the wire is notched in the empty space between the capillaries to initiate the breaking of the junction. See text for more details.*

Figure S2 shows a scheme of the samples used for our MCBJ measurements. They are made from Au wire (250 μm diameter, 99.99%,

Goodfellow) glued into two quartz capillaries (fused silica, 1mm inner diameter, Vitrocom) which are then glued onto a phosphorous bronze bending beam. An optical glue (NOA61, Nordland) is used for both bondings. The wire is notched in the empty space between the capillaries to initiate the breaking of the junction. The free-standing part of the Au wire is typically 200 μm for our samples, and the unfilled parts of the capillaries act as a reservoir for the organic solutions. Before use, samples are cleaned in plasma cleaner (ATTO, Diener Electronic) operated with an air pressure of 0.4 mbar at a power of 30W for two minutes.

The separation of the electrodes is controlled by a micrometer step motor (Z-825, Thorlabs) stacked up with a piezoelectric actuator (sensitivity : 216 nm.V^{-1}). Motors and piezo are driven through an input/output board by a dedicated computer interface, which is also used for acquiring data and feed backing. Because the wire is fixed, the actuator motion is demagnified, allowing accurate control of wire stretching. Taking into account a typical push:stretch ratio of 20:1 and the resolution of our 16-bit DAC, one digit corresponds to less than 3 pm, which is ample for this work. As the stability of the MCBJ is a critical parameter for this study, it is operated in the basement of the laboratory on an optical table to ensure optimal isolation from mechanical vibrations in a temperature-controlled environment (temperature variations below 1°C on a 24-hour scale). At low bias ($35 \leq V_{\text{bias}} \leq 140$ mV for this study) and at room temperature, the drift of the electrodes is below 5 pm.s^{-1} after one or two hours of operation.

The molecular junction conductance is derived from the current intensity that flows through the junction, measured using a home-made current/voltage converter with a logarithmic trans-conductance gain following the design proposed by U. Dürig et al.⁴ This converter allows measurements from the 100pA

range (noise level of 10pA on a 10 kHz bandwidth) up to the mA range, and it is operated at a constant temperature of 20°C. Prior to measurements, the converter is carefully calibrated with a series of precision resistors (1,10,100 MΩ and 1 GΩ 0.1% resistors). These calibration data are then used to calculate the current or conductance values corresponding to the output voltage. The junction, in series with a 1 kΩ ballast resistor to avoid saturation of the trans-impedance amplifier, is biased using a 6V lead battery. The voltage output of the trans-impedance amplifier is recorded using a 16-bit ADC, operated at a sampling frequency of 4096 Hz. Fresh millimolar solutions of molecules in DMSO are prepared and immediately used for measurements.

Measurement and analysis protocol.

To ensure cleanliness of the contacts, samples are broken in pure solvent (here DMSO). They are operated for one or two hours at a typical current set point of 200 pA before measurements begin, to allow mechanical relaxation of the bending beam, and thus stabilization of the electrode distance. We then feed the sample with 10 μL of solution and set a current set point in the sub nA range. This current imposes the distance between the gold electrodes, and after stabilization, the feedback loop controlling the electrode separation is disabled. We then observe the temporal evolution of the current flowing through the contact. A connection or disconnection of a molecule between the 2 electrodes is expected to induce a sharp change (stepwise) in the current. If we do not observe such events, the feedback is enabled, and the set point is increased (reducing electrode separation). These operations are repeated until we observe abrupt current jumps. Taking advantage of thermal diffusion and electromigration, at room temperature, the nano-contact self-organizes at atomic level and naturally explores the most stable configurations around the average chosen conductance value. During these periods we record the temporal evolution of the current flowing through the

contact. We operate the piezo actuator only if the current falls below 100 pA or rise above 100nA. The recording of the current is interrupted when the piezo actuator is active. Figure S3 illustrates a 8s recording of the current flowing through a junction filled with a millimolar solution of molecule **B** in DMSO, operated at a bias voltage of 35 mV. This recording exhibits a random telegraphic signal associated to numerous molecule connection/disconnection events in the contact, as demonstrated in a previous publication.⁵ Current histogram clearly illustrates the discrete nature of current jumps and the most likely values of the current. Such histograms presented below are all constructed using the rule suggested by D.P. Doane for data binning,⁶ in order to be able to compare histograms constructed from datasets of different sizes.

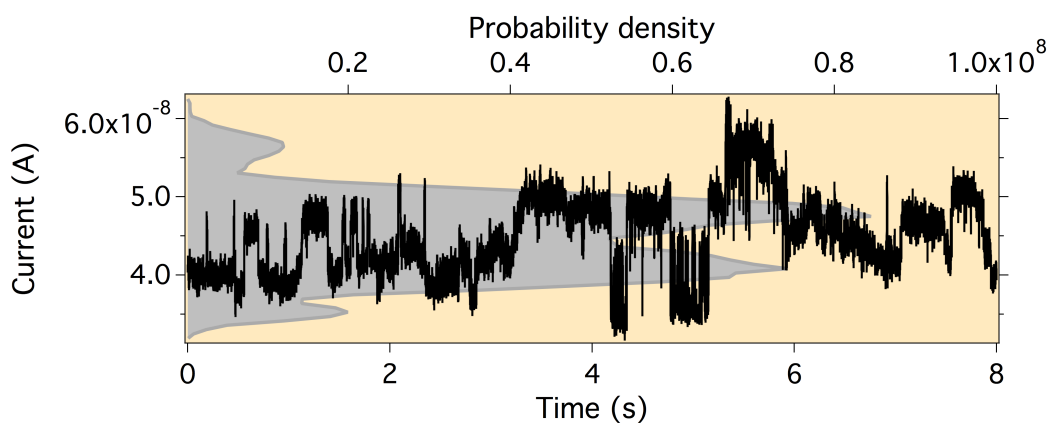
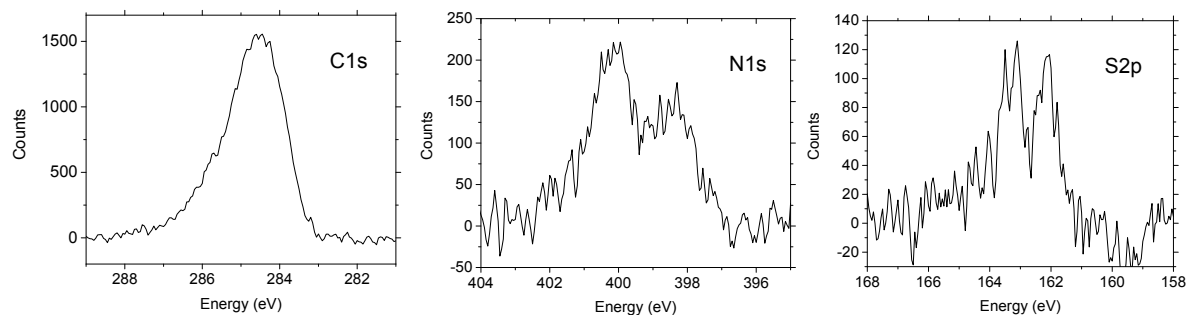


Figure S3 : Spontaneous evolution of the current of a molecular contact formed from a millimolar solution of molecule **B** in DMSO. A 35 mV bias is applied to the junction. The electrode separation is fixed with a set-point current of 1 nA before the regulation feedback is disabled (see text for more details). Current (black line) is recorded. A histogram of the current (gray) clearly indicates the most probable current values.

III. XPS measurements.

SAM molecule A



SAM molecule B

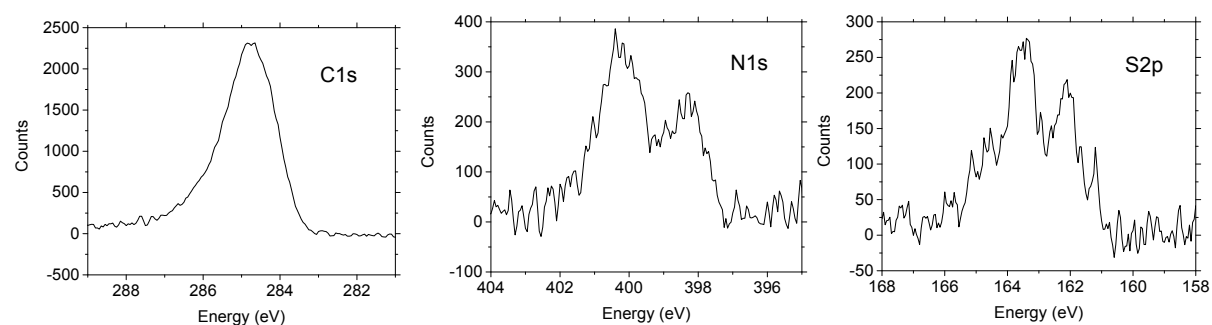


Figure S4. C_{1s} , $S_{2p_{3/2}}$ and N_{1s} spectra of SAMs **A** and **B**.

	C_{1s}	$S_{2p_{3/2}}$ (*)	N_{1s}	S/C	N/C
SAM A	284.4	162.1, 163.2	400.2, 398.4	0.05 (0.06)	0.11 (0.18)
SAM B	284.8	162.1, 163.7	400.4, 398.3	0.09 (0.1)	0.15 (0.2)

Table S1. Peak position (eV) of C_{1s} , $S_{2p_{3/2}}$ and N_{1s} and atomic ratios of elements (expected values from the molecule structures in brackets).

As expected, the S2p spectra of SAMs **A** and **B** (Fig. S5) were composed by 2 contributions of equal intensities (each of them constituted by the 2 components $S_{2p_{3/2}}$ and $S_{2p_{1/2}}$, $\Delta = 1.16\text{eV}$, intensity ratio = 0.51). The first one located at low

binding energy (162.1eV) was associated to S-Au bond, the second one at higher binding energy corresponding to the free thiol end-group.

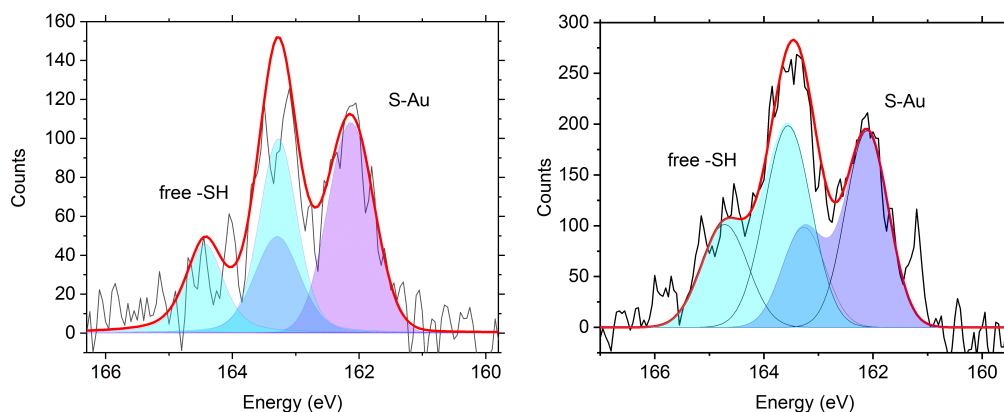


Figure S5. Deconvolutions of $S2p$ spectra for SAMs **A** (left) and **B** (right).

The interpretation of $N1s$ spectra (Fig. S6) for SAMs **A** and **B** is more delicate. Usually 2 signals in a 1:1 intensity ratio are expected for each imidazole rings attributed to pyridinic ($=N-$) and pyrrolic ($-NH-$) nitrogens.⁷⁻⁸ In the case of anilines, it is not rare to observe the presence of hydrogen-bonds and/or the protonated form $Ar-NH_2/NH_3^+$ in the 401-402eV region.⁹⁻¹⁰ Here, for the SAM **A**, 3 bands are observed at 398.4eV, 400.2eV, and 401.7 eV corresponding to imine ($-N=C$), tertiary amine ($-N<$) and protonated/H-bonded nitrogens ($-NH_2/NH_3^+$), respectively. A ratio of 4 ($-N< + NH_2/NH_3^+$) for 2.2 ($-N=C$) is measured, which is closed to the expected value (i.e. 4 amine-type N for 2 imine-type N), knowing that photodamaging by X-rays analysis of amine terminal group into unsaturated imine adducts is also possible.¹¹

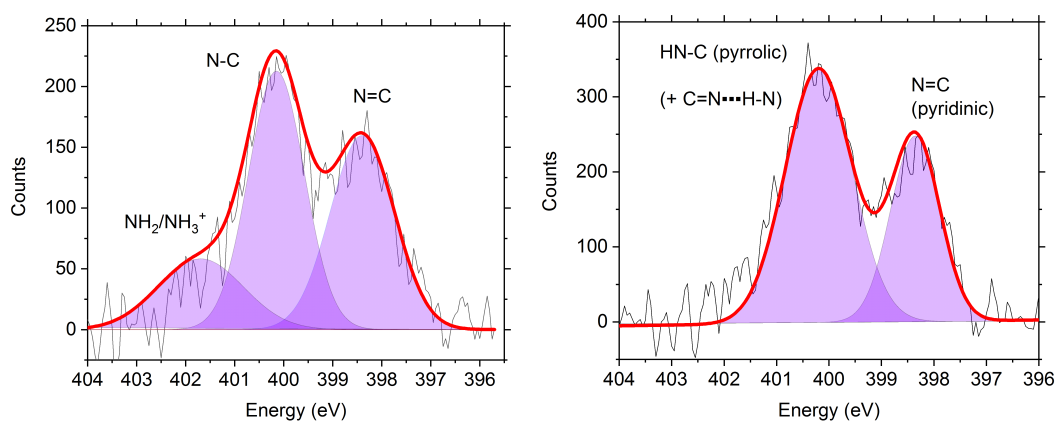


Figure S6. Deconvolutions of N1s spectra for SAMs **A** (left) and **B** (right).

In SAM **B**, the N1s signal has 2 unequal components (1:0.54 intensity ratio instead of the expected 1:1 ratio) observed at 398.3eV (pyridinic N) and 400.4eV (pyrrolic N). In the literature, N1s signals with unequal areas were also observed in polybenzimidazole polymers¹²⁻¹³ or in graphene functionalized by benzimidazole.¹⁴ An explanation could be a difference in X-ray sensitivity of pyridinic nitrogens compared to pyrrolic nitrogens. Another hypothesis to explain the preponderance of the pyrrolic form would be the presence of hydrogen bonding between the pyridinic and pyrrolic nitrogens ($C=N\cdots H-N$) or due to H-bonds with residual water molecules included in the monolayer ($C=N\cdots H-O$).¹⁵ Due to this complexity of N1s spectra for SAM **A** and **B**, it was not possible to clearly identify the signals observed in the presence of acid and base.

IV. Measurements on $^{TS}\text{Au}/\text{SAM}/\text{C-AFM}$ tip junctions.

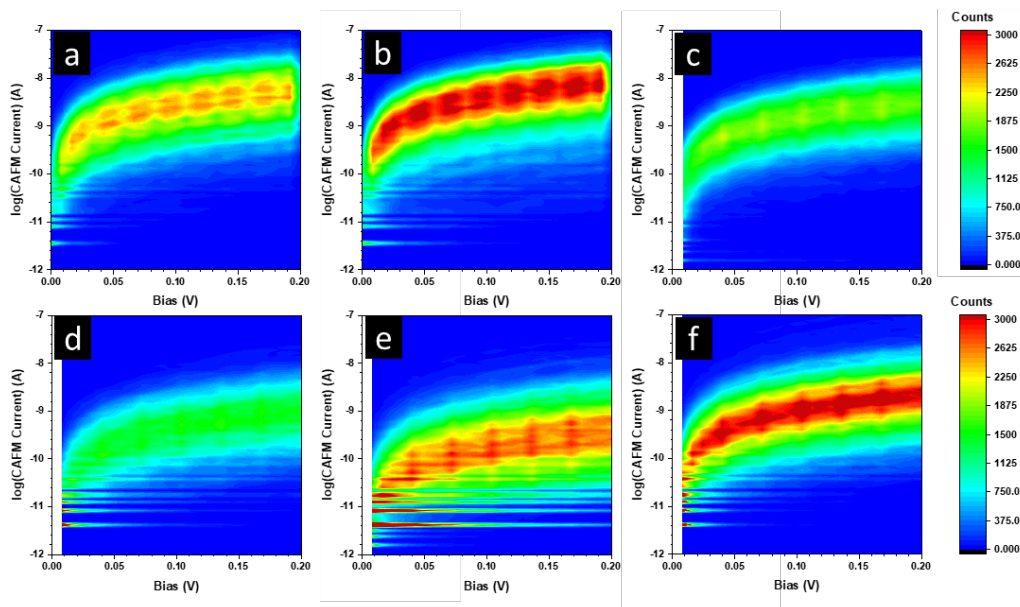


Figure S7. 2D histograms of the current-voltage curves (I - V) for $^{TS}\text{Au}/\text{SAM}/\text{C-AFM}$ tip for (a) pristine SAM A (4515 traces) (b) neutral SAM A (5403 traces); (c) protanated SAM A (3802 traces); (d) pristine SAM B (3492 traces) (e) neutral SAM B (7676 traces) and (f) protanated SAM B (6752 traces).

	NMJs		^{TS} Au/SAMs	
	log μ (log A)	log σ	log μ (log A)	log σ
mol. A - pristine	n.m.	n.m.	-8.32 ± 0.02 (4.78x10 ⁻⁹ A)	0.57 ± 0.05
- protonated	-8.07 ± 0.02 (8.51x10 ⁻⁹ A)	0.33 ± 0.02	-8.81 ± 0.01 (1.55x10 ⁻⁹)	0.36 ± 0.01
- neutral	-7.54 ± 0.01 (2.88x10 ⁻⁸ A)	0.05 ± 0.01	-7.86 ± 0.01 (1.38x10 ⁻⁸)	0.69 ± 0.02
mol. B - pristine	n.m.	n.m.	-9.08 ± 0.01 (8.32x10 ⁻¹⁰ A)	0.59 ± 0.02
- protonated	-7.38 ± 0.01 (4.17x10 ⁻⁸ A)	0.29 ± 0.01	-8.69 ± 0.01 (2.04x10 ⁻⁹ A)	0.50 ± 0.01
- neutral	-7.78 ± 0.02 (1.66x10 ⁻⁸ A)	0.51 ± 0.03	-9.51 ± 0.02 (3.09x10 ⁻¹⁰ A)	0.69 ± 0.02

Table S2. Fitted parameters (mean values and standard deviations) of the log normal distributions for NMJs and ^{TS}Au/SAMs junctions. In brackets: the mean current in A. (n.m. =not measured).

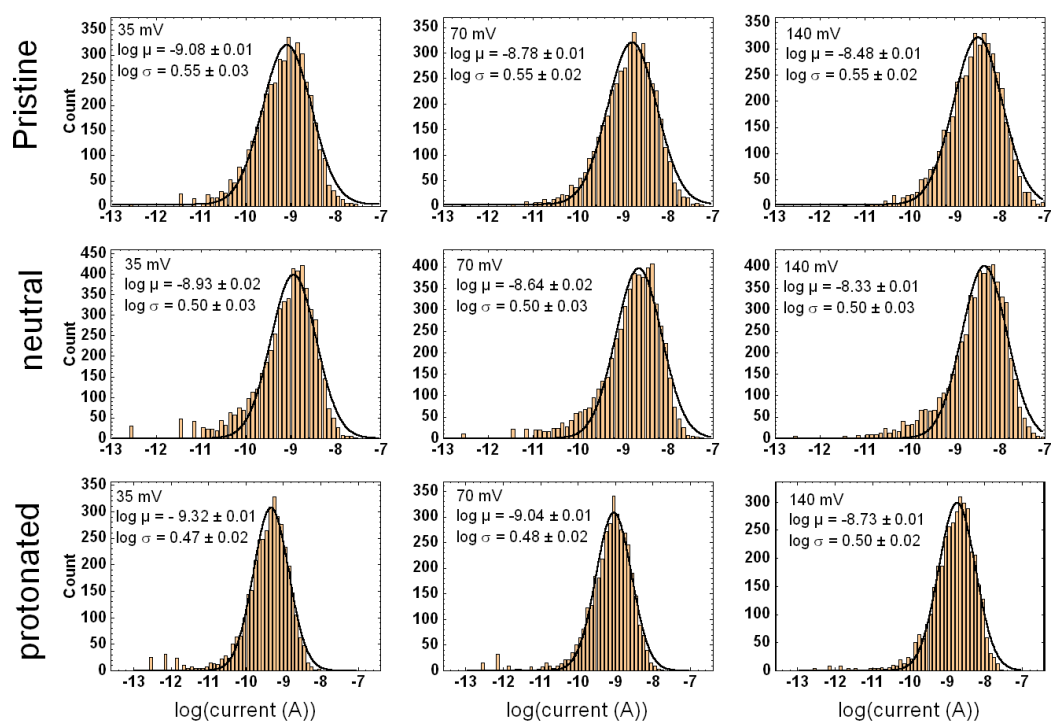


Figure S8. Current histograms of the SAM of molecule A at 35, 70 and 140 mV (from data in Fig. S7a-c) for the pristine, protonated and after converted back to the neutral state.

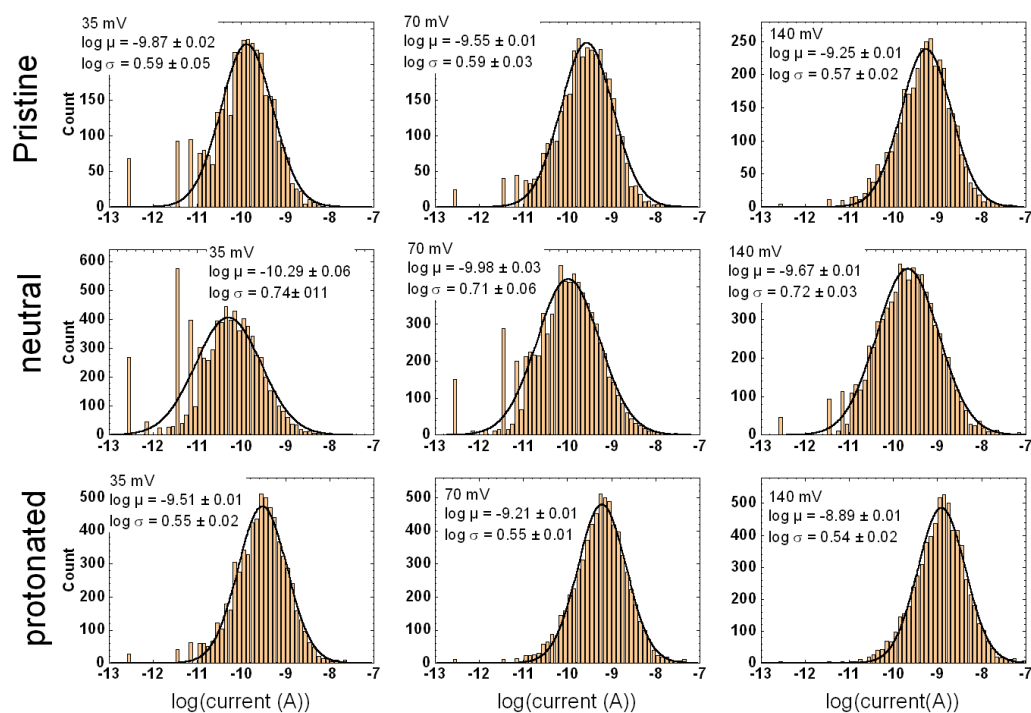


Figure S9. Current histograms of the SAM of molecule **B** at 35, 70 and 140 mV (from data in Fig. S7a-c) for the pristine, protonated and after converted back to the neutral state.

Bias (mV)	A pristine	A protonated	A neutral	B pristine	B protonated	B neutral
35	3.1×10^{-4}	1.8×10^{-4}	4.2×10^{-4}	5.0×10^{-5}	2.1×10^{-4}	1.9×10^{-5}
70	3.0×10^{-4}	1.7×10^{-4}	4.2×10^{-4}	5.1×10^{-5}	1.1×10^{-4}	2.0×10^{-5}
140	3.1×10^{-4}	1.7×10^{-4}	4.2×10^{-4}	5.2×10^{-5}	1.1×10^{-4}	5.7×10^{-5}
200	3.1×10^{-4}	9.7×10^{-5}	9.0×10^{-4}	5.4×10^{-5}	1.3×10^{-4}	2.1×10^{-5}

Table S3. Conductances for the SAMs (in unit of G_0) at 35, 70, 140 and 200 mV for molecules **A** and **B** for the pristine, protonated and after converted back to the neutral state (conductances are the mean currents from the peaks of the current histograms - Figs 1, S8 and S9, divided by the applied voltage).

V. C-AFM on NMJs.

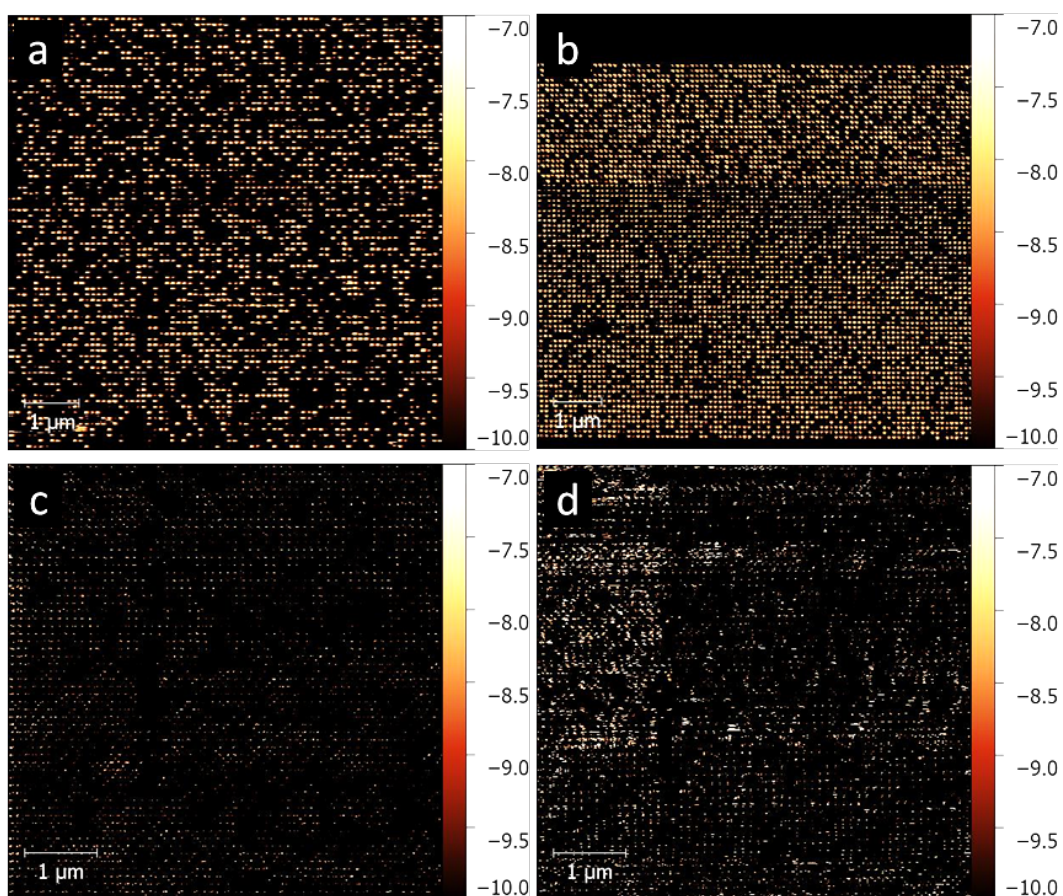


Figure S10. Current image (bright spots are the current value of each NMJ - the scale is in log of the current measured in ampere) obtained by C-AFM (loading force 10 nN and $V_{bias} = 200$ mV) on NMJs with **(a)** neutral molecules **A** (2456 nanodots); **(b)** protonated molecules **A** (2445 nanodots); **(c)** neutral molecules **B** (1154 nanodots) and **(d)** protonated molecules **B** (1634 nanodots).

VI. MCBJ measurements.

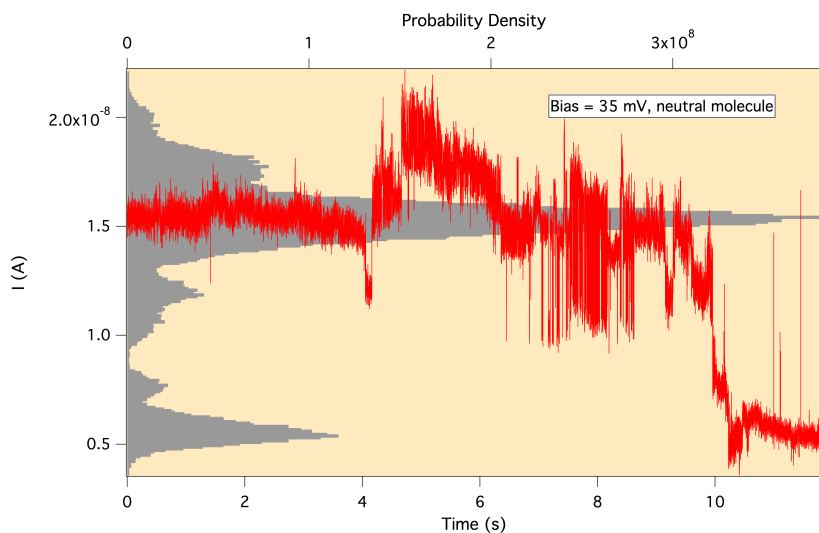


Figure S11. Current vs. time evolution (red) and corresponding current histogram (grey) of molecular junction formed from a millimolar solution of molecule **B** (neutral) in DMSO. A 35 mV bias is applied to the junction. The electrode separation is fixed with a set-point current of 1 nA before the regulation feedback is disabled (see text for more details). Current (black line) is recorded. A histogram of the current (gray) clearly indicates the most probable current values.

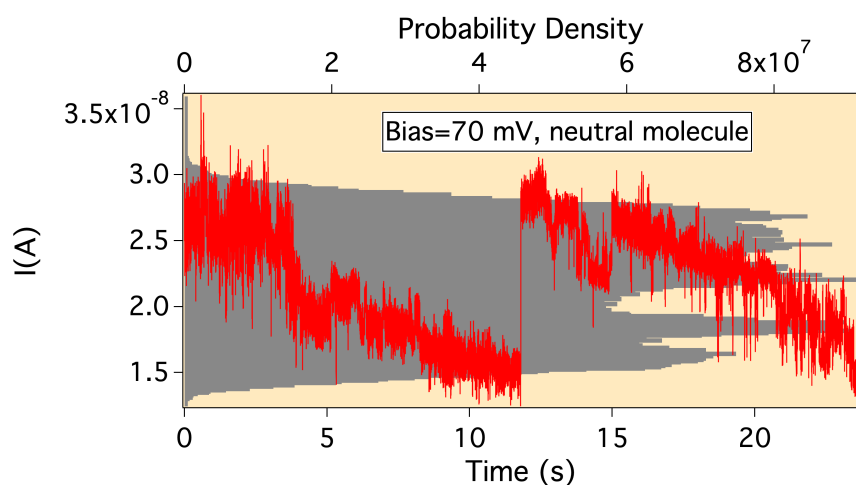


Figure S12. Current vs. time evolution (red) and corresponding current histogram (grey) of molecular junction formed from a millimolar solution of molecule **B** (neutral) in DMSO at $V_{bias} = 70$ mV.

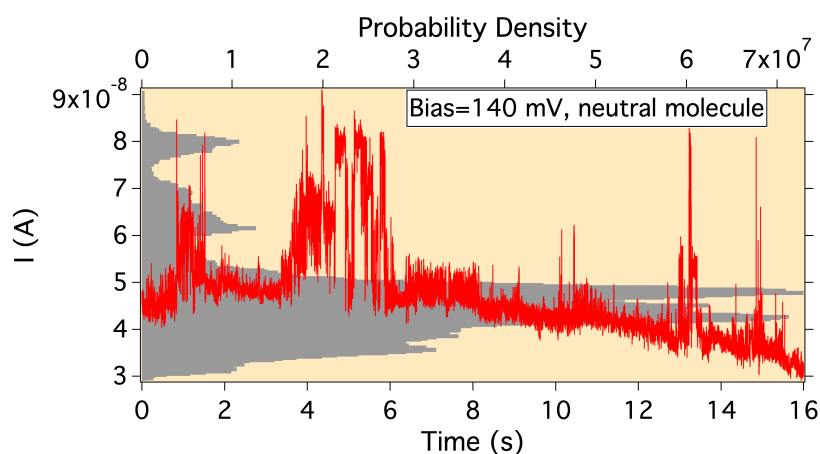


Figure S13. Current vs. time evolution (red) and corresponding current histogram (grey) of molecular junction formed from a millimolar solution of molecule **B** (neutral) in DMSO at $V_{bias} = 140$ mV.

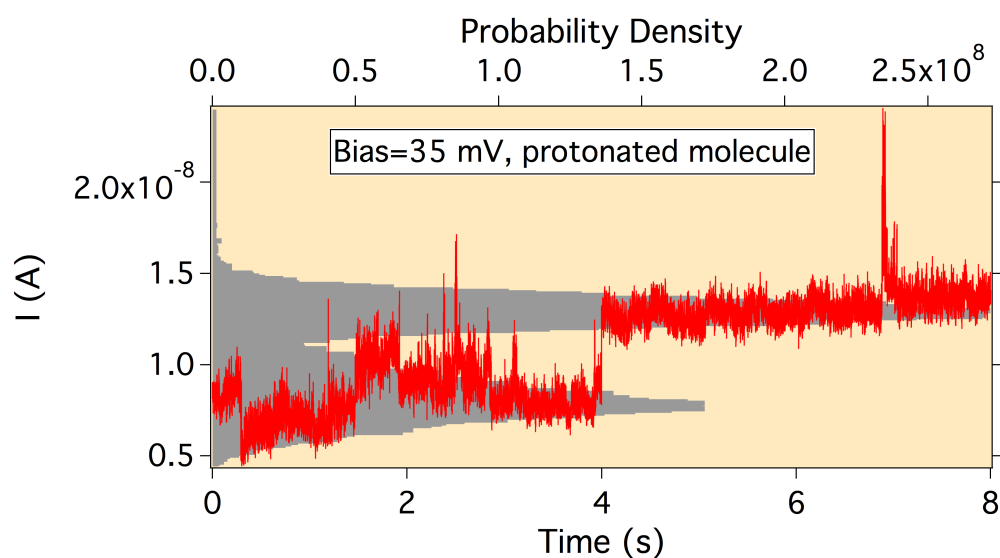


Figure S14. Current vs. time evolution (red) and corresponding current histogram (grey) of molecular junction formed from a millimolar solution of molecule **B** (protonated) in DMSO at $V_{bias} = 35$ mV.

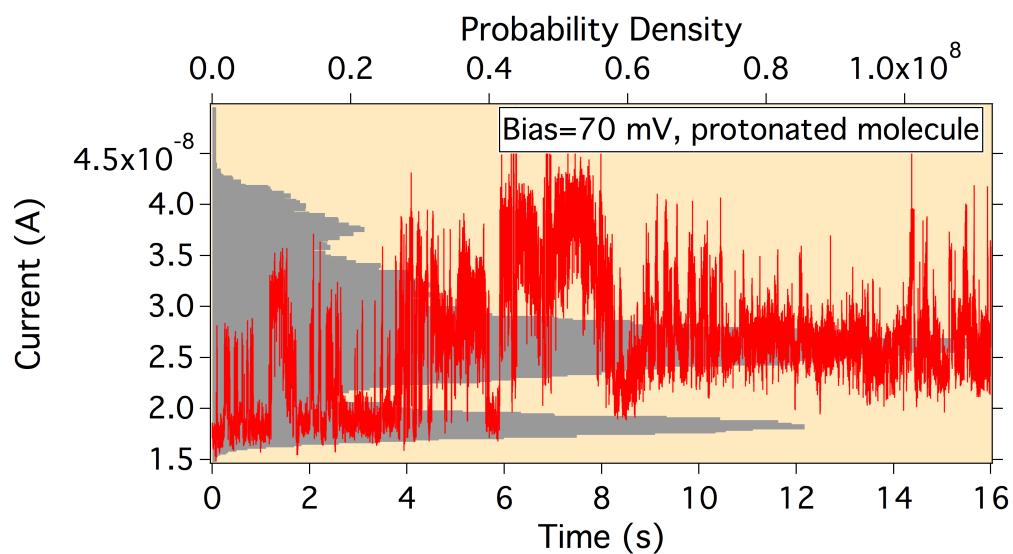


Figure S15. Current vs. time evolution (red) and corresponding current histogram (grey) of molecular junction formed from a millimolar solution of molecule **B** (protonated) in DMSO at $V_{bias} = 70$ mV.

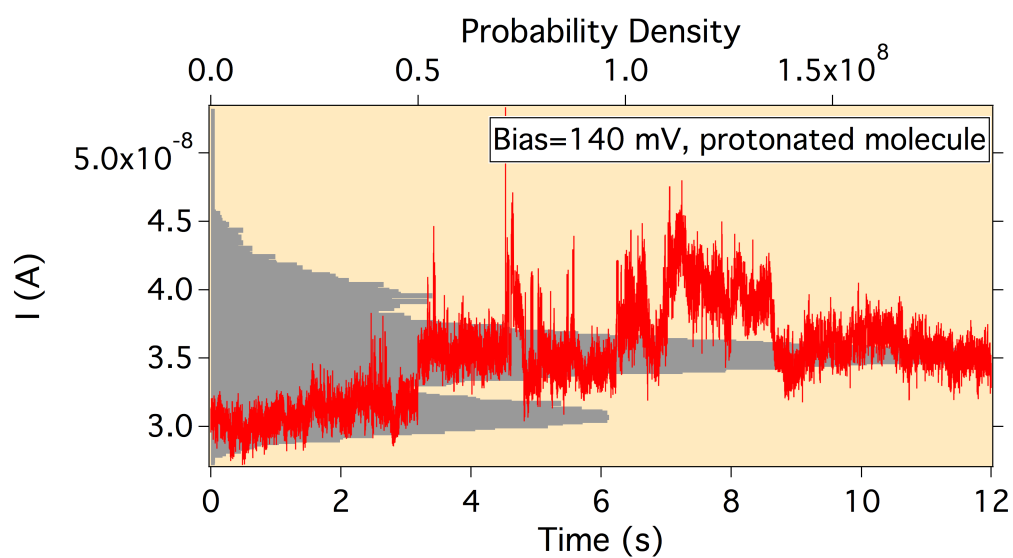


Figure S16. Current vs. time evolution (red) and corresponding current histogram (grey) of molecular junction formed from a millimolar solution of molecule **B** (protonated) in DMSO at $V_{bias} = 140$ mV.

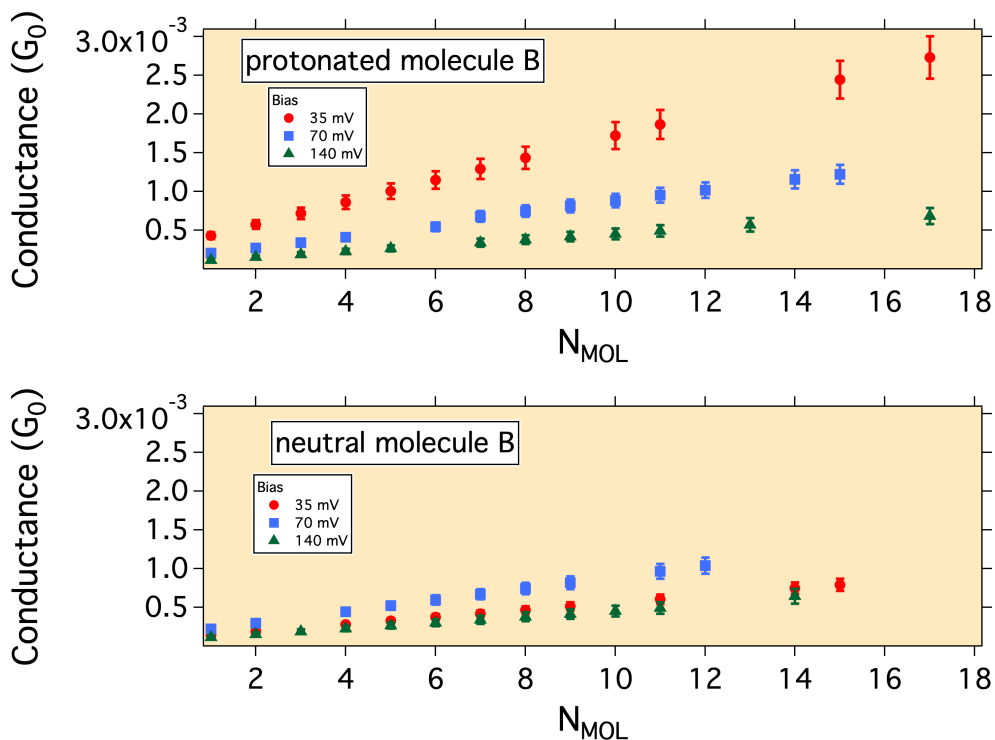


Figure S17. Conductance values of the peaks observed in the histograms of currents versus a number of molecules (up panel: protonated molecule **B** from Figs. S14-S16, down panel: neutral molecule **B**, from Figs. S11-S13). A linear fit gives the G_{MOL} values reported in table 2 (main text) for the 3 applied voltages.

Conductance values are given in conductance quantum units, G_0 .

VII. Modeling, molecule in gas phase

For the modeling of the protonation, we used a cluster model where the protonation reaction for the molecule **A** or **B** is empirically defined by:¹⁶



In this cluster approach, the charge transfer is partially implemented (the Mülliken charge estimated by ab-initio calculation of the chlorine atom is $-0.793e$ and $0.330e$ for the hydrogen) and this is clearly a physical limit compared to the

simple chemical picture sketched by the previous equation. To model the protonated molecules, an HCl molecule has been introduced close to the nitrogen atoms corresponding to the most plausible protonation sites, and the protonated states were minimized in terms of total energy.

- Molecule geometry optimizations

Figure S14 shows the optimized geometries for molecules **A** and **B**. The center of the molecule (imidazole) and the two phenyl groups remain planar. The length of both molecules **A** and **B** is 18.9Å. The major difference is observed for the lateral size of the two molecules : 5.1Å for **A** and 16.3Å for **B**. For the unprotonated state of molecule **A** the dihedral angle between the alanine rings and imidazole is near 90°. For both molecules, the imidazole ring presents the most accessible protonation sites with the presence of two non-hydrogenated nitrogen atoms. The introduction of a HCl molecule leads to the formation of N-H bond characterized by a bond length of 1.0764 Å. The N-H bond length is characteristic of a covalent bond. The protonation leads to a H-Cl distance of 1.891 Å larger than the HCl bond of 1.318Å. For the molecule **A**, up to four protonation degrees can be foreseen with the protonation of the nitrogen atoms belonging to the alanine ring as shown in Figure S14 without disturbing the global geometry of the molecule.

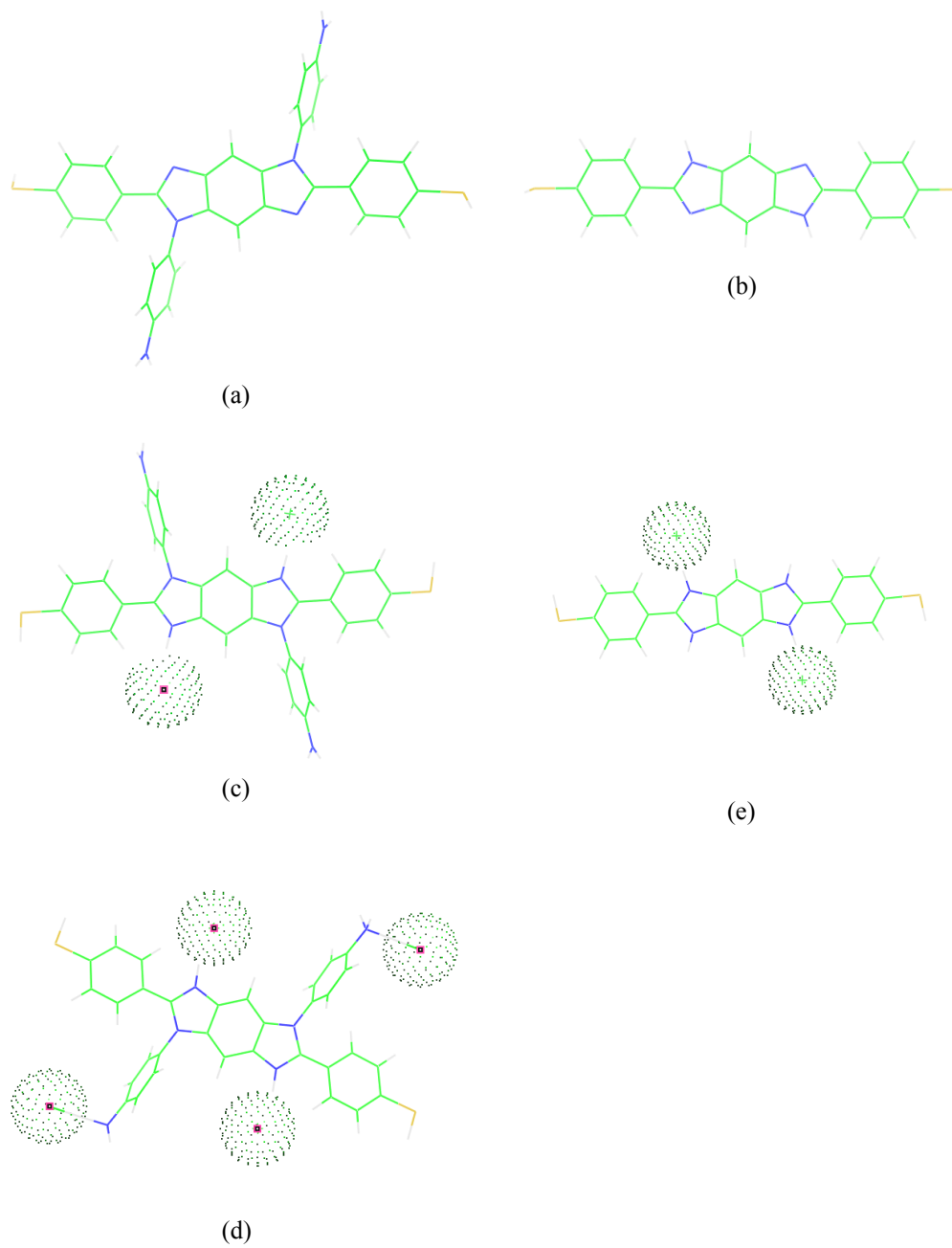


Figure S18. Optimized geometries of (a) unprotonated molecule **A**, (b) unprotonated molecule **B**, (c) protonated molecule **A** with two protons and (d) 4 protons, (e) protonated molecule **B** with two protons.

- Energy levels and molecular orbitals

Figures S15 show the evolution of the HOMO-LUMO gap, the EA and IP of the molecules **A** and **B** as function of the protonation states. For the molecule **A**, most of the HOMO-LUMO band gap variation is obtained when 2 protons are on the imidazole. Protonation of the amine groups have no great effect (see also the molecular orbitals, Figure S16). Basically, the protonation tends to reduce the HOMO-LUMO gap of the molecules and increases the IP and EA. Both the HOMO and the LUMO of molecules **A** and **B** are characterized by highly delocalized wave functions (Figure S16). The protonation of the nitrogen atoms strongly modify the nature of the HOMO as it becomes strongly localized on the protonation sites i.e. on the chlorine counter-ion (Figure S16). On the contrary, the LUMO wave functions remain strongly delocalized on the aromatic cycles.

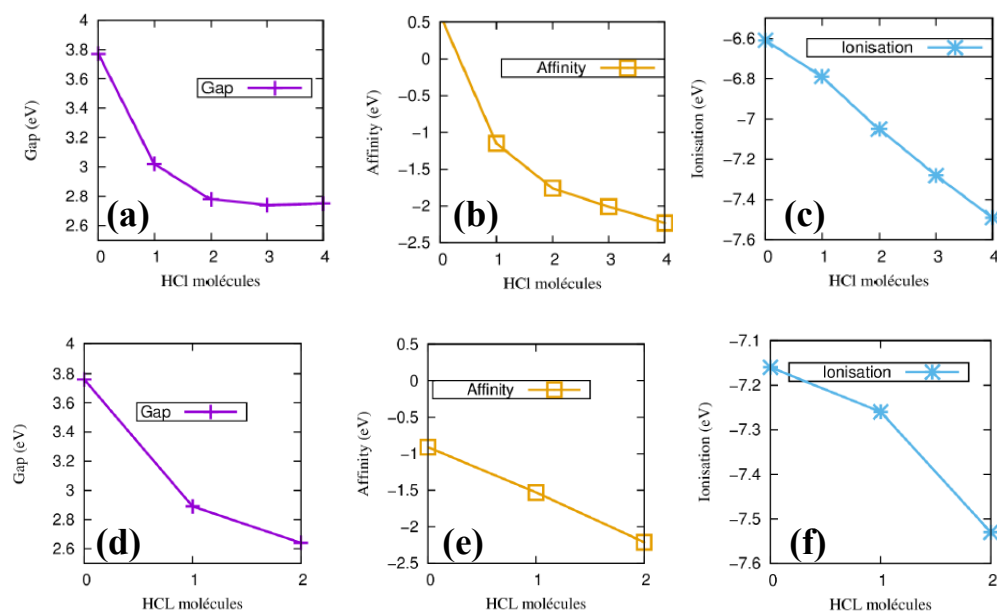


Figure S19. Evolution of (a) the HOMO-LUMO gap, (b) electron affinity and (c) ionization potential of molecule **A** versus the protonation state. Evolution of (d) the HOMO-LUMO gap, (e) electron affinity and (f) ionization potential of molecule **B** versus the protonation state.

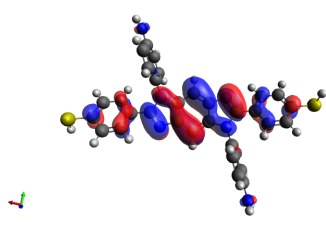
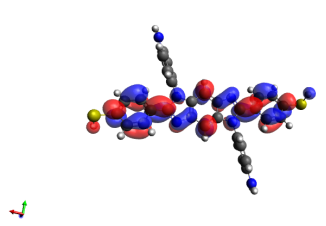
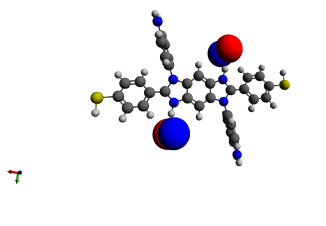
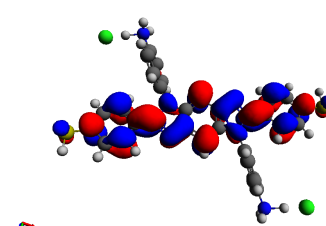
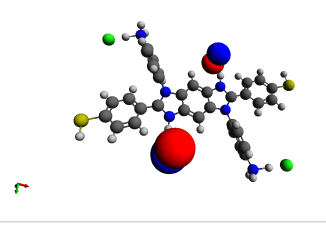
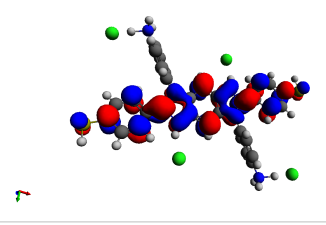
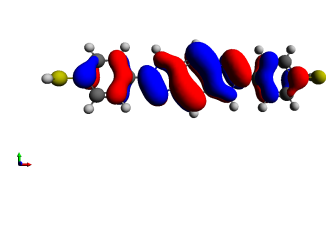
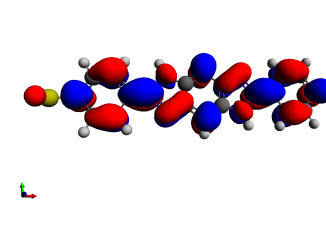
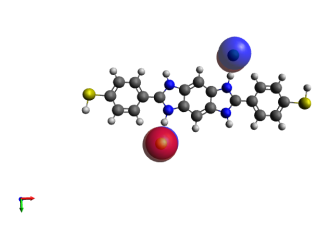
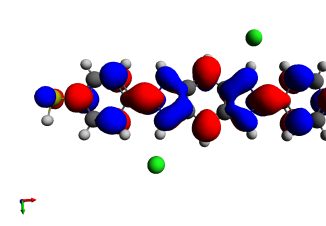
	HOMO	LUMO
molecule A		
molecule A + 2H ⁺		
molecule A + 4H ⁺		
molecule B		
molecule B + 2H ⁺		

Figure S20. HOMO and LUMO wave functions.

- Optical properties

The optical properties of the two molecules were calculated by Time Dependent Density Functional Theory (TDDFT) calculations using the B3LYP functional. Only vertical transitions are considered and the activate space considered correlates 12 electrons with 12 orbitals. For the molecule **A** (respectively **B**), the major optical transition takes place at 346 nm (357 nm, respectively) in good agreement with the measurements of the precursor (Figure S1) with an oscillator strength of 0.9 (respectively 1.28). As shown in Figure S17, upon protonation, a bathochromic shift to 387 nm (385 nm, respectively), i.e. an increase of 41 nm (respectively 28 nm) is observed in qualitative agreement with the experimental observation (Figure S1). This corresponds to a relatively small reduction of the optical gap for molecule **A** (respectively **B**) which is reduced from 3.58 eV to 3.2 eV (respectively from 3.47 to 3.2 eV).

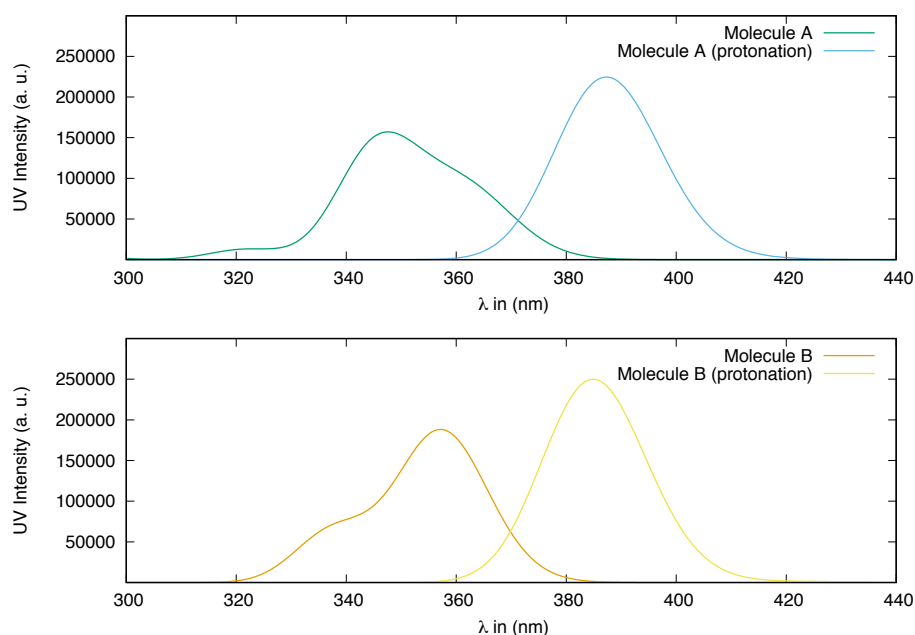


Figure S21. TDDFT simulation of the optical spectrum for molecules **A** and **B** with and without protonation. The calculations indicate that the introduction of localized states near the HOMO degrades the intensity of the optical oscillator

*and the activated occupied states. The active optical transition would be HOMO-6 → LUMO. Protonation states considered are the highest possible for the two molecules (i.e. 4 for **A** and 2 for **B**).*

VIII. Modeling electron transport in metal/molecule/metal junction.

To model the behavior of a metal/molecule/metal junction, we attach the geometry-optimized molecule to gold via the thiol anchor groups. In this case we bind the terminal sulfur atom to a hollow site on a (111) gold surface and the optimum Au-S distance is calculated to be 2.3 Å. The hydrogen atom contacted to the sulfur is removed. An extended molecule is then constructed to consist of 6 layers of (111) gold each containing 25 atoms. Using the DFT code SIESTA,¹⁷ a Hamiltonian describing the extended molecule is generated using the following parameterization. A double- ζ plus polarization basis set, energy cut off=150 Rydbergs, norm conserving pseudopotentials, and the GGA method¹⁸ to describe the exchange correlation. The zero bias transmission coefficient $T(E)$ is then calculated using this Hamiltonian, via the GOLLUM code.¹⁹ The room temperature conductance can then be evaluated from the Landauer formula,

$$G = \frac{2e^2}{h} \int_{-\infty}^{\infty} dE T(E) \left(\frac{-df(E)}{dE} \right)$$

Where, $f(E)$ is the Fermi-Dirac distribution, e is the electronic charge and h is Planck's constant. The electrical current is evaluated using the equation,

$$I = \frac{2e}{h} \int_{-\infty}^{\infty} dE T(E) [f_L(E) - f_R(E)]$$

Where f_L and f_R are the Fermi-Dirac distributions in the left and right lead respectively.

-Conductance of neutral molecules A and B

Figure S18 shows the calculated conductance through molecules **A** and **B** for the geometry given in Figure 6. Here the HOMO resonances of the two molecules lie at similar positions relative to the SIESTA predicted Fermi Energy E_F^0 . This is in disagreement with the calculated behavior in the gas phase (Fig. S15), where the HOMO level of **B** lies at a lower energy. This can be attributed to the thiol anchor groups (after losing a hydrogen) pinning the HOMO close to the Fermi energy in this calculation.

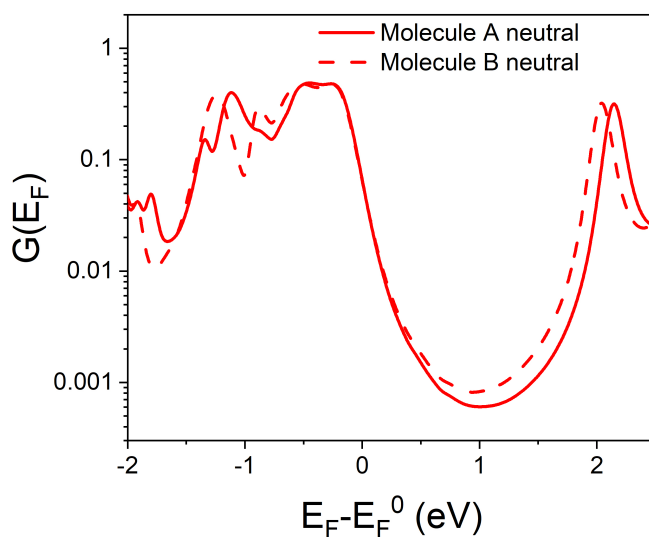


Figure S22. Electrical conductance of the deprotonated molecules **A** and **B**.

-Electron transport through a protonated molecule

Protonation of the molecule, by adding hydrogen atoms at the nitrogen sites, causes the molecule to become charged. Therefore, counter ions, which here are chlorine are needed to balance the charge i.e. making the added hydrogen atoms

H^+ and the chlorine atoms Cl^- . To achieve this within SIESTA requires analysis of the electron distribution using a Mulliken population analysis. To form a Cl^- ion requires the number electrons on the chlorine atom to increase by one (here we define N as the number of electrons added to the chlorine atom). The charge on the chlorine atom can be controlled by varying the cut-off radius in the basis set. Here we set the $Cl-H$ distance to be 3\AA . Figure S19 shows the transmission for the protonated molecule **B**, for different values of N on the counter ions. When there are no counter ions, the LUMO resonance lies directly at the Fermi energy as expected for a charged system (cyan line). The addition of the counter ion shifts the position of the Fermi energy towards the middle of the HOMO-LUMO gap and the extent of the shift is controlled by the value of N on the counter ions. Here $N=0.7$ (blue line) and $N=1.0$ (black line).

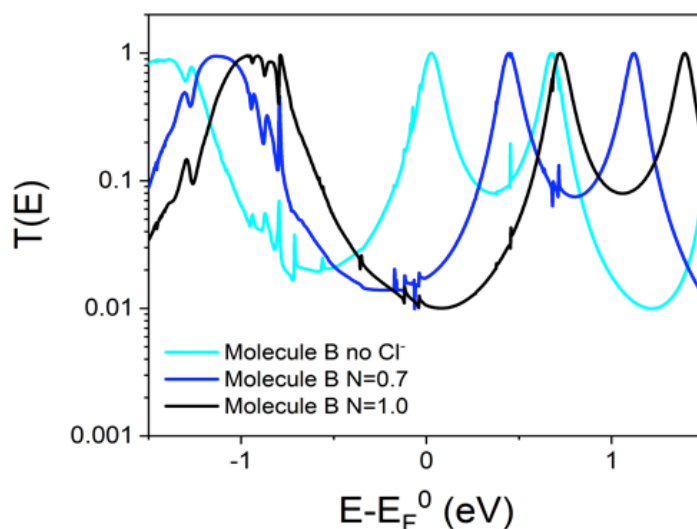


Figure S23. Transmission coefficient $T(E)$ for the protonated molecule **B** when they are no Cl^- counter ions (cyan), when the number of electron N on the Cl atom =0.7 (blue) and when $N=1$ (black).

-Tilt angle

The SAM of molecule **A** has a smaller thickness than **B**, which suggests the molecule is tilted. Figure S20 shows the calculation for a tilt angle of 60° relative to the surface normal (the gold-gold separation is now 1.4nm). The resulting behavior is similar to that for the linear geometry in figure 6, with the transmission decreasing when the molecule is protonated.

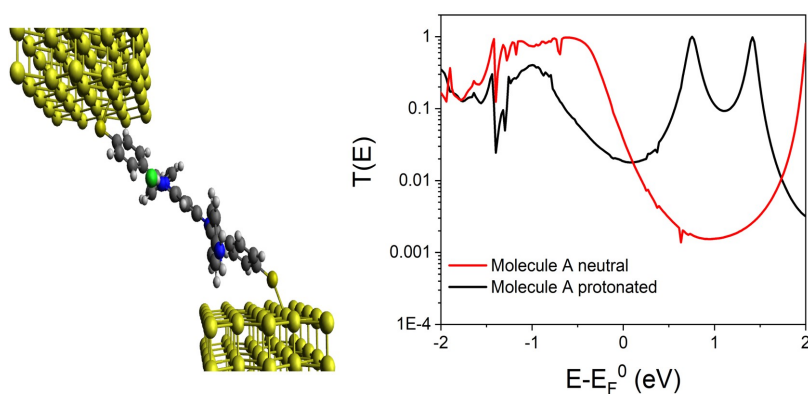


Figure S24. Zero bias transmission coefficient $T(E)$ for molecule **A** tilted at an angle of 60° away from the normal.

-Transport through NH_2 anchor groups in Molecule A

Molecule **A** contains NH_2 groups, which may couple to the gold electrodes. We calculate for this geometry, where the N-Au distance is 2.4 (figure S21). The resulting transmission shows that the off-resonance values are much lower than the equivalent molecule binding through the thiols. At the Fermi energy the value of $T(E)$ is approximately 3 orders of magnitude lower. This is due to the ring rotation, which is approximately 90° to the central core, and suggest that these groups play a minimal role in the electron transport.

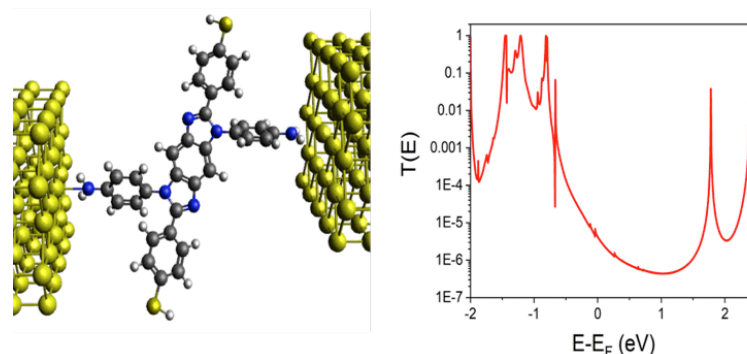


Figure S25. (left) Geometry of molecule *A* contacted to gold electrodes through the NH_2 groups and (right) the corresponding zero bias transmission coefficient $T(E)$.

IX. References

1. Chan, Y.-H.; Lin, J.-T.; Chen, I.-W. P.; Chen, C.-H., Monolayers of Diphenyldiacetylene Derivatives: Tuning Molecular Tilt Angles and Photopolymerization Efficiency via Electrodeposited Ag Interlayer on Au. *J Phys Chem B* **2005**, *109* (41), 19161-19168.
2. Foucoin, F.; Caupène, C.; Lohier, J.-F.; Sopkova de Oliveira Santos, J.; Perrio, S.; Metzner, P., 2-(Trimethylsilyl)ethyl Sulfoxides as a Convenient Source of Sulfenate Anions. *Synthesis* **2007**, *2007* (09), 1315-1324.
3. Muller, C. J.; Van Ruitenbeek, J. M.; de Jongh, L. J., Conductance and supercurrent discontinuities in atomic-scale metallic constrictions of variable width. *Phys. Rev. Lett.* **1992**, *69* (1), 140-143.
4. Dürig, U.; Novotny, L.; Michel, B.; Stalder, A., Logarithmic current-to-voltage converter for local probe microscopy. *Rev. Sci. Instrum.* **1997**, *68* (10), 3814-3816.
5. Gil, M.; Malinowski, T.; Iazykov, M.; Klein, H. R., Estimating single molecule conductance from spontaneous evolution of a molecular contact. *J. Appl. Phys.* **2018**, *123* (10), 104303.

6. Doane, D. P., Aesthetic Frequency Classifications. *The American Statistician* **1976**, *30* (4), 181-183.
7. Nolting, D.; Ottosson, N.; Faubel, M.; Hertel, I. V.; Winter, B., Pseudoequivalent Nitrogen Atoms in Aqueous Imidazole Distinguished by Chemical Shifts in Photoelectron Spectroscopy. *J Am Chem Soc* **2008**, *130* (26), 8150-8151.
8. Lu, W.; Zhang, G.; Li, J.; Hao, J.; Wei, F.; Li, W.; Zhang, J.; Shao, Z.-G.; Yi, B., Polybenzimidazole-crosslinked poly(vinylbenzyl chloride) with quaternary 1,4-diazabicyclo (2.2.2) octane groups as high-performance anion exchange membrane for fuel cells. *Journal of Power Sources* **2015**, *296*, 204-214.
9. Graf, N.; Yegen, E.; Gross, T.; Lippitz, A.; Weigel, W.; Krakert, S.; Terfort, A.; Unger, W. E. S., XPS and NEXAFS studies of aliphatic and aromatic amine species on functionalized surfaces. *Surface Science* **2009**, *603* (18), 2849-2860.
10. Meyerbroeker, N.; Waske, P.; Zharnikov, M., Amino-terminated biphenylthiol self-assembled monolayers as highly reactive molecular templates. *The Journal of Chemical Physics* **2015**, *142* (10), 101919.
11. Song, X.; Ma, Y.; Wang, C.; Dietrich, P. M.; Unger, W. E. S.; Luo, Y., Effects of Protonation, Hydrogen Bonding, and Photodamaging on X-ray Spectroscopy of the Amine Terminal Group in Aminothiolate Monolayers. *The Journal of Physical Chemistry C* **2012**, *116* (23), 12649-12654.
12. Sugama, T., Hydrothermal degradation of polybenzimidazole coating. *Materials Letters* **2004**, *58* (7), 1307-1312.
13. Hao, J.; Jiang, Y.; Gao, X.; Xie, F.; Shao, Z.; Yi, B., Degradation reduction of polybenzimidazole membrane blended with CeO₂ as a regenerative free radical scavenger. *Journal of Membrane Science* **2017**, *522*, 23-30.
14. Ai, W.; Zhou, W.; Du, Z.; Du, Y.; Zhang, H.; Jia, X.; Xie, L.; Yi, M.; Yu, T.; Huang, W., Benzoxazole and benzimidazole heterocycle-grafted graphene for

- high-performance supercapacitor electrodes. *Journal of Materials Chemistry* **2012**, *22* (44), 23439-23446.
15. Heinrich, T.; Darlatt, E.; Lippitz, A.; Müller, S.; Schalley, C. A.; Unger, W. E. S., Systematic XP and NEXAFS spectroscopy studies of (ter-)pyridine-terminated self-assembled monolayers and their addressability for functional molecules. *Journal of Electron Spectroscopy and Related Phenomena* **2019**, *233*, 28-37.
16. Singh, U. C.; Kollman, P. A., A combined ab initio quantum mechanical and molecular mechanical method for carrying out simulations on complex molecular systems: Applications to the CH₃Cl + Cl⁻ exchange reaction and gas phase protonation of polyethers. *Journal of Computational Chemistry* **1986**, *7* (6), 718-730.
17. Soler, J. M.; Artacho, E.; Gale, J. D.; Garcia, A.; Junquera, J.; Ordejon, P.; Sanchez-Portal, D., The SIESTA method ad initio order-N materials simulation. *Journal of Physics Condensed Matter* **2002**, *14* (11), 2745.
18. Perdew, J. P.; Burke, K.; Ernzerhof, M., Generalized Gradient Approximation Made Simple. *Physical Review Letters* **1996**, *77* (18), 3865-3868.
19. Ferrer, J.; Lambert, C. J.; García-Suárez, V. M.; Manrique, D. Z.; Visontai, D.; Oroszlany, L.; Rodríguez-Ferradás, R.; Grace, I.; Bailey, S. W. D.; Gillemot, K.; Sadeghi, H.; Algharagholy, L. A., GOLLUM: a next-generation simulation tool for electron, thermal and spin transport. *New Journal of Physics* **2014**, *16* (9), 093029.